Chemical Engineering Journal 469 (2023) 143964

Contents lists available at ScienceDirect

Chemical Engineering Journal

journal homepage: www.elsevier.com/locate/cej

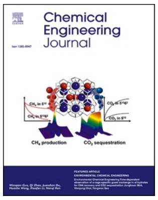

Recovering electrical energy from forward osmosis process through amorphous silicon oxide crosslinked vanadium pentoxide-reduced graphene oxide membrane

Priyamjeet Deka [a], Sonali Roy [b], Tukhar Jyoti Konch [b], Barsha Rani Bora [b], Raktim Gogoi [b], Arindom Bikash Neog [b], Krishnaraajan Sundararajan [b], Senthilmurugan Subbiah [c,*], Kalyan Raidongia [b,*]

[a] *School of Energy Science and Engineering, Indian Institute of Technology Guwahati, Guwahati 781039, India*
[b] *Department of Chemistry, Indian Institute of Technology Guwahati, Guwahati 781039, India*
[c] *Department of Chemical Engineering, Indian Institute of Technology Guwahati, Guwahati 781039, India*

ARTICLE INFO

Keywords:
FO-coupled energy process
Electrochemical energy-generation
Forward osmosis
Nanofluidic
Reduced graphene oxide
Vanadium pentoxide

ABSTRACT

Forward osmosis (FO) is a promising technology for energy-efficient water treatment but suffers from the drawback of reverse solute flux which often results in energy loss. Recent research has been directed toward reducing energy consumption and improving efficiency in the FO process. However, there remains a significant gap in utilization the inevitable reverse solute flux. Our study introduces an innovative approach to minimize energy consumption by transforming this reverse solute flux into sustainable electricity. Here, we fabricated membranes using two-dimensional flakes of vanadium pentoxide (VO) and reduced graphene oxide (r-GO) and cross-linked with amorphous silicon oxide (aSiO). The optimized VO-aSiO-rGO membrane showcases a remarkable ability to recover nearly 26% of the power applied for liquid pumping, exhibiting a significant advancement in the FO process. The membrane also outperforms commercial CTA-based FO membranes by achieving superior water fluxes (~45 $L/m^2.h$) and low specific reverse salt fluxes (SRSF) (~0.13 g/L), indicating its superior separation efficiency for concentration applications. Moreover, the VO-aSiO-rGO membrane demonstrated stable performance with a water flux of 28.5 $L/m^2.h$ over 40 h of continuous operation. Additionally, it successfully generated output voltage and current values up to 293 mV and 32.2 μA, respectively, with a 10^6 fold salinity gradient, leading to a power density of ~ 4.72 $W.m^{-2}$. The study also explored energy-recovering possibilities and crystal production in realistic scenarios using different concentrations of tea as the feed solutions. The results of this work not only address the critical gap in the efficient use of energy in the FO process but also provide a significant breakthrough towards sustainable and efficient water treatment technologies with integrated energy recovery systems.

1. Introduction

The forward osmosis (FO) process, due to its energy efficiency and low membrane fouling propensity, has become a focal point in applications such as the concentration of high-value products, and wastewater treatment [1,2]. However, the economic viability of the FO process for producing low-cost end products is hindered by the challenges in recovering draw solution (DS). The cost of draw regeneration drives the capital expenditures (CAPEX) and operating expenditures (OPEX) of the FO process, and most of the techno-economic studies reported in the literatures either assume that the sea water can be used as DS or without regeneration of conventional DS [3,4]. Hence, the financial payback time for any FO process depends on the water flux of the FO membrane. The higher water flux can lead to lower payback time, reducing the system's overall coast and energy consumption. However, commercial FO membranes and polymer based membrane exhibit lower water flux, high reverse solute flux (RSF), fouling propensity and high cost which limit their applications [5]. Moreover, the current technologies demand high energy and cost, as indicated by recent statistics [6–8]. Therefore, well-packed permselective nanofluidic

---

* Corresponding authors.
E-mail addresses: senthilmurugan@iitg.ac.in (S. Subbiah), k.raidongia@iitg.ac.in (K. Raidongia).

https://doi.org/10.1016/j.cej.2023.143964
Received 19 April 2023; Received in revised form 30 May 2023; Accepted 4 June 2023

membranes prepared by assembling two-dimensional nanomaterials possess high surface density and exhibit the potential to reduce costs by simultaneously increasing the water flux and reducing the reverse salt flux [9,10].

Scattered efforts that holistically address the water and energy issues are visible in the recent literature. For instance, the bio-electrochemical reactions of microorganisms in microbial cells have shown potential for simultaneous energy and pure water production [11,12]. However, maintaining the pace of such enzymatic processes is a nontrivial task. Similarly, Park et al demonstrated the possibility of simultaneous water and energy production from the reverse osmosis (RO) process using the ion-selective membranes, recovering nearly 50% of the pumping energy [13]. However, maintaining the integrity of electrode–membrane assemblies in the high-pressure system is a challenging task, which is a primary bottleneck in areas like fuel cells and electrolyzer [14,15]. Therefore, the search is on for alternative systems or methods along with fabrication of novel membranes that could simultaneously address the issues of water and energy.

The salinity energy harvesting process, namely pressure retarded osmosis (PRO) [16], reverse electrodialysis RED [17], and capacitive mixing (CM) [18] are extensively studied for standalone energy generation applications, considering the viability of producing more than 15% of the total global energy by mixing river and seawater at seawater. Both processes are unsuccessful for commercial deployment due to non-availability of the energy efficient membrane. As discussed above, both standalone energy generation and FO process have economic limitations; therefore, combining both FO and energy generation processes in a single membrane process may be the optimistic approach to achieve better economics.

Coating of nanomaterials on conventional FO membranes enhanced the water flux and ion selectivity by increasing the charge density [19,20], and such coated membranes can do both FO and energy generation simultaneously. Among different 2D material-based membranes, VO possess the highest surface charge and lowest resistance to ionic transport [21,22]. Similarly, r-GO-based membranes are known to possess superior stability, selectivity and anti-fouling properties in an aqueous medium [23,24]. The optimized membrane can exhibit higher water flux and low reverse solute flux (RSF) and simultaneously can generate electrical energy to compensate for the energy consumption during the FO process.

Novelty of our study lies in demonstrating the potential for simultaneous energy generation and the FO-based concentrating process using lamellar nanofluidic membranes and creating a novel platform for research towards developing a nearly self-sustaining FO system with minimum application of external energy. Our optimized membrane significantly enhances the water flux and reduces the reverse salt flux (RSF), leading to simultaneous electrical energy generation over prolonged operational hours. Additionally, this robust coating of 2D nanomaterials has shown excellent stability in deionized (DI) water as well as in acidic and basic mediums. Findings of this research could find applications in multiple areas like incorporation of biowaste into circular bioeconomy, extraction of high value products from microalgae, and remediation of acid mine drainage [25–28].

2. Experimental sections

2.1. Synthesis of VO dispersion and VO-aSiO membrane

The VO nanosheets were synthesized by stirring VO powder with H_2O_2 in ice-cold conditions (5–10°C) [29]. Typically, 2.4 g VO powder was dispersed in 25 ml deionized (DI) water, followed by the addition of 25 ml of 50 % H_2O_2. The addition of H_2O_2 produced vigorous bubbling, yielding dark-brown precipitation, which slowly turned into a thick gel. The gel was diluted with DI water to prepare dispersions of required concentrations.

For the preparation of VO-aSiO membrane, 40 μl bis[3-(triethoxysilyl) propyl] tetrasulfide (Bis) was stirred with 25 ml ethanol for 1 h and 13 ml of VO dispersion (15 mg/ml) was mixed with Bis solution and heated at 80 °C for 3 h under refluxed conditions. After reacting with Bis, the dark brownish-coloured VO dispersion turned into dark greenish coloured aSiO-VO dispersion. Finally, the solution was filtered through a PTFE membrane of 0.1 μm pore size and dried in ambient conditions to obtain the freestanding VO-aSiO membrane. The digital images of the dispersions and respective membranes are shown in supplementary Fig. S1.

2.2. Fabrication of VO-aSiO-rGO membrane

Typically, a thin layer of GO flakes is coated on top of a nylon support membrane via vacuum filtering 30 ml aqueous dispersion of graphene oxide (GO) (0.033 mg/ml). The VO-aSiO dispersion (4 ml of 1 mg/ml) was vacuum filtered through the GO-coated nylon membrane. The tri-layered membrane was then dried inside a desiccator for 24 h, followed by heating under vacuum at 150 °C for 2 h. Digital images of thus prepared membranes (VO-aSiO-rGO) and GO membranes are shown in supplementary Fig. S2.

2.3. Generation of electricity from concentration gradient

The VO-aSiO-rGO/nylon membrane was placed as a separator between two chambers of an electrochemical device. Two Ag/AgCl electrodes connected to a Keithley-2450 sourcemeter instrument were dipped in the reservoir solutions. The output voltage and current values were recorded using Keithley-2450 digital sourcemeter, by filling one of the chambers with an aqueous solution of 10^{-6} M KCl, and the KCl concentration of other chambers was varied from 10^{-5} M to 1 M. The current–voltage (I-V), and current–time (I-T) graphs were recorded under each salinity gradient and correspondingly power density was calculated by using Equation (1).

$$P = V^{*}I/A \tag{1}$$

Where V is the output voltage in Volt (V), I is the output current in Ampere (A) and A is the membrane area in m^2.

2.4. Membrane performance evaluation

The performance of fabricated rGO, VO-aSiO and VO-aSiO-rGO membranes was investigated in a lab-scale FO set-up (effective area of 4 cm^2) under a controlled environment. Details and schematic representation (Fig. S5) are presented in section 1.6 of supporting information. The draw solution (DS) and feed solution (FS) tanks were circulated through the FO test cell with a definite flow rate using plunger pumps. The water flux was calculated by measuring the change the draw solution's weight change using a weighing balance (model-XD/XR) with accuracy of ± 0.01 g. The reverse solute flux (RSF) of different salt concentrations was measured by using the Hanna conductivity meter (model H15321). A digital image of the full FO setup coupled with the sourcemeter is shown in supplementary Fig. S6.

3. Results and discussions

3.1. Characterization of GO flake and VO nanosheet

The bi-layer nanoporous membrane is prepared by coating commercial nylon membranes with aSiO crosslinked 2D sheets VO and GO (VO-aSiO-GO). While GO is prepared through the modified hammer method, VO sheets are exfoliated from bulk powder by treating them with ice-cold H_2O_2 at 5–10 °C [20,30]. Detailed fabrication techniques and characterization of the GO, VO and VO-aSiO sheets are discussed in the supplementary section 1.4. In short, the lateral dimensions of GO are in the range of 500 to 2000 nm, and that of VO varies between 300 and 800 nm, see AFM images in supplementary Fig. S3(B). The average

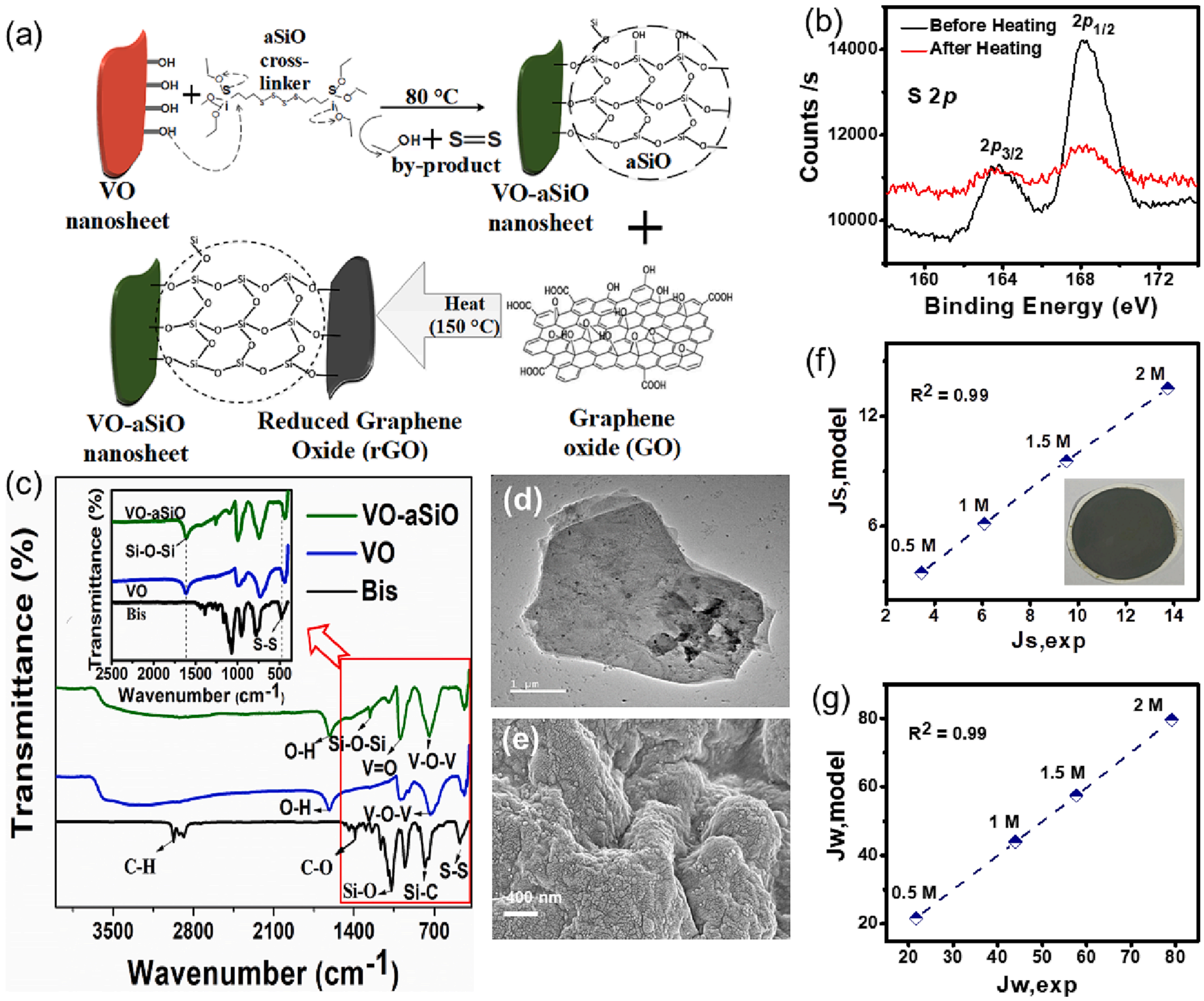

Fig. 1. Basic characterizations of membranes: (a) Schematic illustration of the VO-aSiO-rGO membrane fabrication process. (b) XPS peak of sulphur 2p in VO-Bis mixture before and after heating at 80 °C. (c) FTIR spectra of VO-aSiO, VO and Bis samples. (d) FETEM image of VO-aSiO nanosheet, and (e) FESEM surface morphology of VO-aSiO membrane. The intrinsic parameters of the VO-aSiO-rGO membrane: (f) reverse solute flux (g/m^2.h) (inset image shows VO-aSiO-rGO membrane), and (g) water flux (L/m^2.h) with DS of different concentrations (0.5 M–2 M) with DI water as the FS.

height of GO, and VO flakes are ~ 5 nm and 6 nm, respectively. The zeta potentials of both GO and VO are negative with a magnitude of 31 mV and 45 mV, respectively, consistent with the earlier reports [31,32]. The large negative zeta potentials values indicate the existence of high-density negative charges on the surface of the 2D sheets. As illustrated in Fig. 1a, pristine VO nanosheets are functionalized with aSiO cross-linker by reacting the same with Bis molecules at 80 °C. After the aSiO coating, the magnitude of the zeta potential of VO is found to decrease from − 45 mV to − 34 mV. The reduction in zeta potential is attributed to the consumption of free surface hydroxyl groups for binding with aSiO linkers generated from the decomposition of Bis molecule. A similar observation is reported by Cheng et al with kaolinite clay [33]. Before heating at 80 °C, the X–ray photoelectron spectrum (XPS) of the VO and Bis mixture showed a doublet energy peak of S 2p centred at 164 eV and 168 eV originating from the S-S group [34]. However, it disappeared after the heat treatment process, suggesting the decomposition of the Bis-molecule, shown in Fig. 1b. The Bis-molecule decomposes by releasing ethanol and the S-S group leaving behind amorphous SiO [33]. The release of the S-S group and formation of aSiO is also supported by the FTIR analysis. The band centred at 472 cm^{-1} (S-S bond) and 780 cm^{-1} (Si-C group) of the Bis molecule [35] disappeared after the heat treatment process, indicating the release of the S-S group and breakage of the Si-C linkage, respectively. A new peak centred at 1256 cm^{-1} appeared in the IR spectrum of the VO-aSiO membrane that represents the Si-O-Si linkage which proves the successful grafting of SiO moieties onto the surface of VO nanosheets via chemical bonding [36], see Fig. 1c. The dark patches of the VO-aSiO sample observed in the FETEM examination also indicate the deposition of aSiO on the VO surface shown in Fig. 1d. Moreover, the surface morphology of the VO-aSiO membrane in FESEM shows a rough and fluffy-like surface (see Fig. 1e), indicating the formation of agglomerated nanospheres of amorphous oxides of silicon after decomposition of Bis molecules.

The VO-aSiO-rGO membrane was prepared by vacuum filtering VO-aSiO dispersion through GO coated nylon membranes followed by heating at 150 °C. The annealing process reduces oxygenated functional groups of GO and helps to strengthen the membrane through π-π interactions between the graphitic regions of adjacent rGO nanosheets [37,38]. During the vacuum filtration and heating process, the cross-linking of aSiO also extends to rGO layers via bonding between the terminal -Si-OH group of VO-aSiO and oxygen functional groups of rGO through hydrolysis, which is evident from the Si-O-C band at 1050 cm^{-1} in the IR spectrum of VO-aSiO-rGO in supplementary Fig. S3B(d). A similar mechanism was reported by Zhang et al, where the hydrolysis of tetra-ethyl-ortho-silicate (TEOS) led to the formation of silica nanoparticles, which interacted with GO nanosheets through the conversion of C=O bonds on GO to Si-O-C bonds upon reaction with TEOS [39]. The existence of crosslinking and π-π interactions in the VO-aSiO-rGO membrane is also indicated by the outstanding stability of the

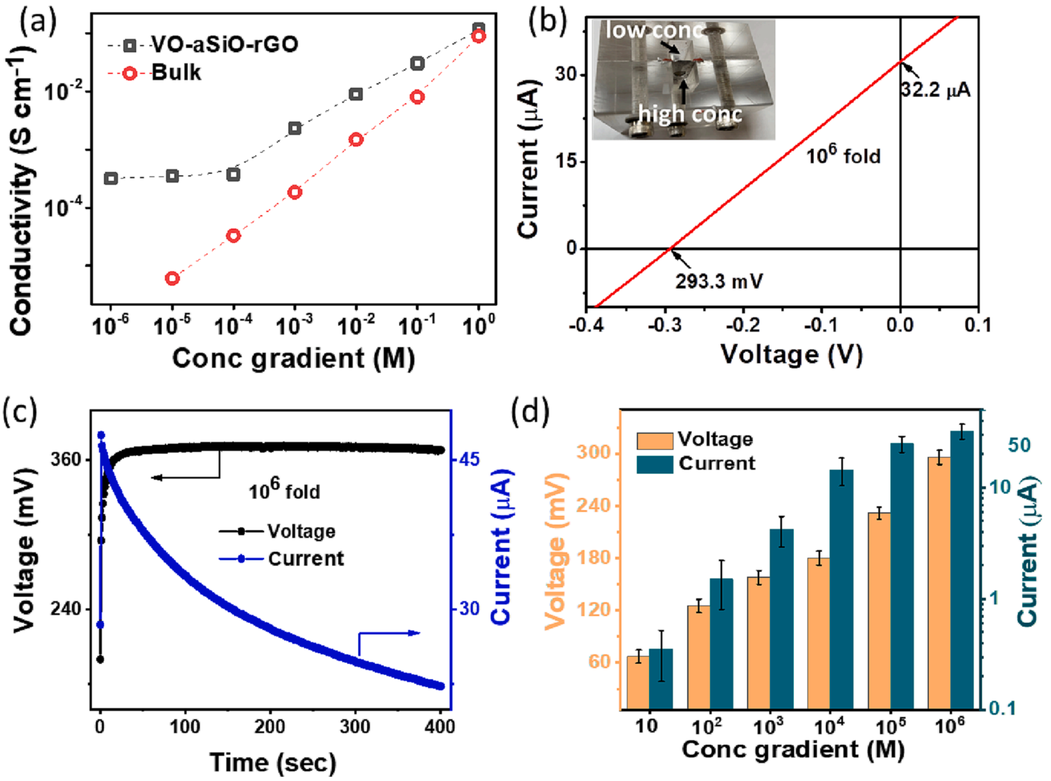

Fig. 2. Generation of electricity from concentration gradients: (a) Surface charge governed ionic conductivity plot, and (b) I-V graph of VO-aSiO-rGO membrane with 10^6 fold concentration gradient of KCl (inset image shows a digital image of an electrochemical device). (c) Output voltage and current as a function of time with 10^6 fold concentration gradient. (d) Comparison of output voltage and current at different concentration gradients.

membrane in aqueous environments. Soaking in water for more than 60 days did not deteriorate its mechanical and chemical integrity. Under similar conditions, both pristine GO and rGO membranes started breaking down within 10 days. The stability of the VO-aSiO-rGO membrane is also studied under acidic and basic conditions. It is seen that even after 90 days of soaking in 10^{-3} M and 10^{-4} M HCl and 10^{-3} M and 10^{-4} M NaOH solution, the membrane's structural integrity is strong enough without deteriorating its mechanical strength.

The intrinsic parameters like water permeability (L_p), solute permeability (B) and structural parameter (S) for optimized VO-aSiO-rGO membrane are estimated in the active layer facing draw solution (ALDS) mode of the FO process [40]. The pure water permeability (L_p, L/m^2.h.bar), solute permeability coefficient (B, L/m^2.h), structural parameter (S, nm), and mass transfer coefficient for DS and FS (K_d, m.h^{-1}) of VO-aSiO-rGO membrane are estimated to be 39.9 ± 0.004, 6.57 ± 0.065, 472500, 0.74 ± 0.008 and 18.02 ± 0.043, respectively. The pure water permeability, solute (NaCl) permeability coefficient and structural parameters are also determined experimentally. Fig. 1f and Fig. 1g compares experimentally and model predicted water flux and reverse solute flux for 0.5 M–2 M draw solution concentration. It can be observed that both water flux and reverse solute fluxes of the model and experimental data are aligned with R^2 values of around 0.99 confirming the validation of experimental results with the model study. Details of the calculation are shown in supplementary section 1.5.

Table 1
Comparative energy performance of our membrane with other reported literatures.

Membrane	Salinity gradient	Power density (W.m^{-2})	Voltage (mV)	Reference
PEI@GO/CNFs	50 fold	5	158	[41]
MS/AAO	1 μM – 3 M	4.5	96	[42]
TOBC/GO	0.5 – 0.01 M	0.96	121	[43]
CoAl LDH	10^3 fold	0.7	165	[44]
ANFs@MMT	10^4 fold	5.16	197.45	[45]
WS_2/CNF	0.5 – 0.01 M	1.99	55.81	[46]
$Ti_3C_2T_X$	10 μM – 3 M	7.89	280	[47]
VO-aSiO-rGO	10^6 fold	4.75	293	This work

PEI@GO/CNFs = Carbon nanofibers membrane bridged with grapheme nanosheet and hyperbranched polymer, MS/AAO = Mesoporous silica-alumina heterostructure membrane, TOBC/GO = TEMPO oxidized cellulose nanofiber, CoAl LDH = Cobalt Aluminium layer double hydroxide, ANFs@MMT = Aramid nanofibres are intercalated into lamellar montmorillonite membrane, WS_2/CNF = Metallic phase WS_2/ cellulose nanofibre composite membrane, $Ti_3C_2T_X$ = Layered titanium carbide membrane,

To understand the transport characteristics of the VO-aSiO-rGO membrane, a rectangular piece of the same is mounted in between two compartments of an electrochemical device. Ionic conductivities of the membrane are measured by filling the compartments with aqueous KCl solutions. The linear current vs voltage (I-V) curves going through the origin indicate the presence of fluidic channels in the VO-aSiO-rGO membrane that interconnect the electrolyte chambers. The conductivity vs KCl concentration plot shown in Fig. 2a displays two distinct regimes, for bulk-like conductivity and surface-charged-governed conductivity. The occurrence of surface-charged-governed conductivity and XRD reflections in the 2ɵ values at 6.5 Å and 10 Å suggest the existence of molecularly thin 2D nanofluidic channels in the VO-aSiO-rGO membrane as shown in the supplementary Fig. S3(A).

4. Concentration gradient-driven electricity generation

The developed membrane consists of tiny nanofluidic channels that can selectively transport ions and molecules based on their size and charge, providing an ideal means for separating and purifying substances. The fabricated membrane generated electrical energy from a concentration gradient established in the compartments of an

Table 2
Data extracted from experimental measurements under different concentration gradients.

C_{max}/C_{min}	V_{meas} (I = 0) (mV)	V_{redox} (mV)	$V_{osm} = V_{meas} - V_{red}$ (mV)	I_{meas} (V = 0) (μA)	G (μA/V)	$I_{red} = G \times V_{red}$ (μA)	$I_{osm} = I_{meas} - I_{red}$ (μA)	t_+
10	67.6	56	11.6	0.312	4.47	0.25	0.062	0.598
10^2	124	110.5	13.5	1.5	12.4	1.37	0.13	0.557
10^3	158	142	16	4.1	26.7	3.79	0.31	0.545
10^4	180	162	18	14.4	82.4	13.35	1.05	0.538
10^5	235.7	204	31.7	24.8	110	22.44	2.36	0.554
10^6	293	190	103	32.2	91.3	17.34	14.86	0.645

electrochemical device (shown in the inset image of Fig. 2b) and is separated by a VO-aSiO-rGO membrane. The low concentration side is fixed at 10^{-6} M aqueous KCl solution and the high concentration side is varied from 10^{-5} M and 1 M. As expected, the VO-aSiO-rGO membrane generated different open circuit voltage (V_{oc}) and short-circuit current (I_{sc}) from the varying concentration gradients. The system could generate a V_{oc} of 293.3 mV and I_{sc} of 32.2 μA at the maximum concentration gradient. The V_{oc} and I_{sc} vs time curve is shown in Fig. 2c. The related I-V graph for other individual membranes (rGO, VO-aSiO) at 10^4 fold is shown in Fig. S4b, represents lower V_{oc} and I_{sc} as compared to VO-aSiO-rGO membrane. This disparity can be ascribed to the lower surface charged density exhibited by the rGO and VO-aSiO membranes. The declining trend of current can be attributed to the change in the concentration gradient across the chambers (due to the water flux and RSF), and concentration polarization near the membrane. The V_{oc} (at I = 0) and I_{sc} (at V = 0) obtained from I to V curves are found to be increasing with the increasing concentration gradient, as shown in Fig. 2d. The power density is found to be increasing with the increasing concentration gradients, and the highest power density of 4.72 $W.m^{-2}$ is measured at a concentration gradient of 10^{-6}, supplementary Fig. S4c. In Table 1, the output energy performance of VO-aSiO-rGO membrane with other systems reported in recent years.

The V_{oc} obtained in the previous experiment comprises two components, (a) the redox potential due to potential drop at the electrode–electrolyte surface (V_{redox}), and (b) voltage due to selective diffusion of ions (V_{osm}) [48]. Similarly, the I_{sc} values obtained as such have contributions from both ion selective diffusion and V_{redox}. V_{osm} is obtained by subtracting the contribution of V_{redox} from V_{oc} ($V_{osm} = V_{oc} - V_{red}$), and I_{diff} is obtained from $I_{diff} = V_{diff} \times G$, where G is the conductance of the membrane. Transport numbers of cations calculated under each salinity gradient are shown in Table 2.

The V_{redox} itself is measured by using a pair of Ag/AgCl electrodes across the nylon support membrane without having a coating on it. In low-concentration gradients, the experimental V_{redox} values are increasing linearly. However, at higher concentration gradients, it deviates linearly with a reduced slope, as shown in the supplementary Fig. S4a. Similar behaviour is also reported by other authors [49,50] which can be attributed to the following factors. The large pore sizes of nylon support membrane (without coating), due to which, at higher concentration gradient, the ions quickly travel across the chambers minimizing the concentration difference, and inefficiency of Ag electrodes to convert large ionic signals into electrical signals in such a short time.

4.1. *Performance of membranes in the FO process*

The fabricated VO-aSiO-rGO membrane is also explored for the FO process by using a lab-scale FO test cell with an effective area of 4 cm^2. The draw solution (DS) and feed solution (FS) are circulated through the FO test cell with a flow rate of 10 L/h and 20 L/h using plunger pumps, respectively. With 1 M NaCl as the DS and DI water as the FS, in active layer facing draw solution (ALDS) mode, the VO-aSiO-rGO membrane displayed a remarkable 45 $L/m^2.h$ water flux (obtained by measuring the change in weight of draw solution), with a reverse salt flux of 6.1 $g/m^2.h$ (obtained by measuring conductivity). The water and reverse salt flux of the VO-aSiO-rGO membrane are at par with the industrial requirement of the FO process.

The membranes' water flux and reverse salt flux are also studied by changing the compositions of the VO-aSiO loading along with GO loadings together, details are discussed in supporting Fig. S7a-b and Fig. S8a, respectively. In short, the membrane prepared with 1 mg GO and 12 mg VO-aSiO displayed the lowest water flux and reverse salt flux of 9.5 $L/m^2.h$ and 4.1 $g/m^2.h$ respectively. Similarly, the membrane prepared with 0.25 mg GO and 4 mg VO-aSiO displayed the highest water flux and reverse salt flux of 80 $L/m^2.h$ and 70 $g/m^2.h$ respectively. As discussed earlier, the membrane prepared with 1 mg GO and 4 mg VO-aSiO showed a water flux of 45 LMH and reverse salt flux of 6.1 gMH, the same is considered an optimized membrane and used for further studies.

4.2. *Comparative FO performance analysis and stability test*

A commercial CTA-FO, r-GO/nylon, and PSS-doped rGO membrane from our previous study [38] are also operated under conditions similar to that of the VO-aSiO-rGO membrane for comparison. The water flux of VO-aSiO-rGO (45 $L/m^2.h$) is found to be 6, 1.8 and 1.3 times higher than CTA-FO (7.8 $L/m^2.h$), rGO/nylon (26 $L/m^2.h$) and PSS-rGO/nylon (34 $L/m^2.h$) membrane, respectively, as shown in Fig. 3a. The higher water flux of VO-aSiO-rGO membrane is attributed to a lower contact angle (51° vs 80° of rGO membrane) and enlarged inter-layer d-spacing (13.6 Å vs 8 Å of rGO membrane), see supplementary Fig. S3A. Moreover, the RSF values of the VO-aSiO-rGO membrane (6.1 $g/m^2.h$) are found to be lower than that of similar membranes like CTA-FO (8.7 $g/m^2.h$), rGO/nylon (7 $g/m^2.h$) and PSS-rGO/nylon (6.5 $g/m^2.h$), as shown in Fig. 3b. The low RSF of the VO-aSiO-rGO membrane is attributed to the higher negative surface charges of both VO-aSiO (-34 mV) and rGO (-26 mV) layers, resulting in a stronger repulsive force between Cl^- ion and negatively charged membrane by Donnan exclusion [51]. With the addition of VO-aSiO to rGO/nylon membrane (VO-aSiO-rGO), the SRSF of VO-aSiO-rGO decreased by 51.8% from 0.27 g/L of rGO/nylon membrane to 0.13 g/L, shown in Fig. 3c.

An experiment to evaluate the long-term stability of the VO-aSiO-rGO membrane is conducted with 1 M NaCl as DS and DI water as FS in the ALDS mode. Fig. 3d compares the water flux of the VO-aSiO-rGO membrane with that of the rGO membrane for 40 h. During the initial period (first 2 h), rGO and VO-aSiO-rGO membranes exhibited water fluxes of 25 $L/m^2.h$ and 45 $L/m^2.h$, respectively. Though declining trends are observed in the water fluxes of both membranes, the VO-aSiO-rGO membrane maintained a stable water flux of 28.5 $L/m^2.h$ after a day of continuous operation. Moreover, the rate of decrease in the water flux is observed to be lower in the VO-aSiO-rGO membrane as compared to that of the rGO membrane. After conducting the FO experiment for 25 h, both the draw and feed sides are thoroughly cleaned with DI water and osmotic backwashing. After cleaning, the water flux of the VO-aSiO-rGO membrane is increased to 38.5 $L/m^2.h$, while that of the r-GO membrane is increased to 16.3 $L/m^2.h$. The flux recovery ratio (FRR%) of the VO-aSiO-rGO and rGO membranes is calculated to be 85.5% and 65.2%, respectively. The higher FRR% in the VO-aSiO-rGO membrane is attributed to hydrophilic VO-aSiO coating on the rGO layer, which helped in preventing salt penetration from the draw side and mitigating

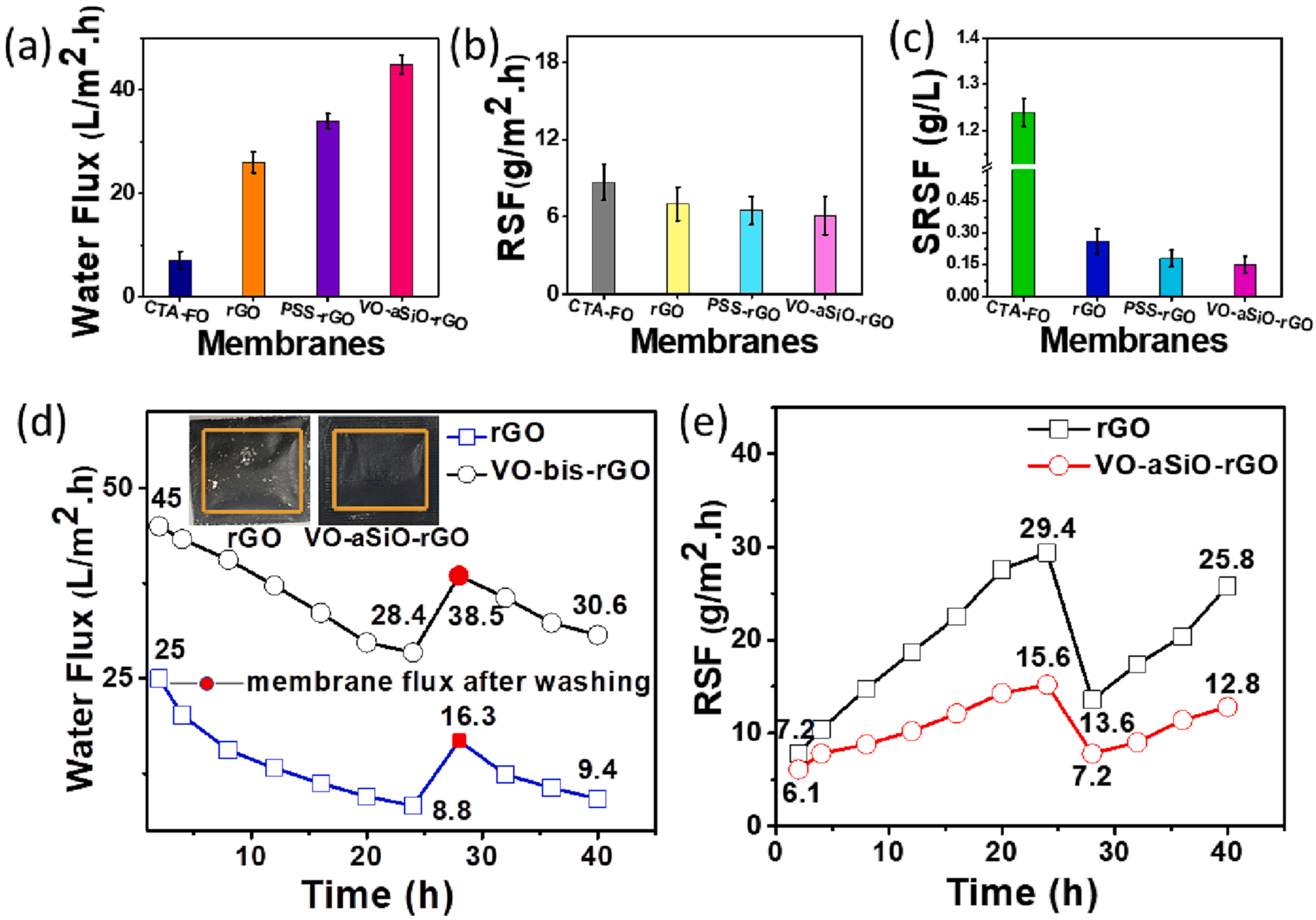

Fig. 3. Comparative FO performance: (a) Water flux, (b) RSF, and (c) SRSF values of CTA-FO, rGO, PSS-rGO and VO-aSiO-rGO membranes coated on nylon substrate measured under identical FO conditions. Long-term stability test of rGO/nylon and VO-aSiO-rGO/nylon membranes with respect to (d) water flux, and (e) RSF with 1 M NaCl as DS and DI water as FS in the ALDS mode (inset shows the images of respective membranes).

internal concentration polarization (ICP) [52].

Similarly, the RSF values for both VO-aSiO-rGO and r-GO membranes are increased with increasing time, but the rate of increment in the VO-aSiO-rGO membrane is found to be lower than that of the r-GO membrane (Fig. 3e), which is again attributed to the higher negative charge of VO-aSiO (-34 mV) flakes as compared to that of rGO (-26 mV) flakes. Another possible reason for the lower RSF of the VO-aSiO-rGO membrane may be due to reduced dilutive external concentration polarization (DECP) with high water flux, i.e. at higher water flux with VO-aSiO-rGO membrane, the draw solution is highly diluted (compared to r-GO membrane), lowering the concentration gradient across the separation layer, which further help to reduce the RSF [53]. Moreover, after prolonged operation, leaching is observed in the rGO membrane but not in the VO-aSiO-rGO membrane. The VO-aSiO-rGO membrane also showed excellent long-term stability (more than 60 days) in DI water and as well as both acidic and basic mediums, as shown supplementary Fig. S9a-b. However, if the membrane is not washed, the water flux reduces as the concentration polarization builds up creating a barrier for permeating water from the feed side to the draw side. However, after a particular duration, the flux reaches a steady state as the effect of concentration polarization gets saturated, as evident from derivative flux value which tends to reach zero. Moreover, the predicted flux plotted by extending the duration infers that the water flux won't decrease below 20 L/m^2.h even after continuing the experiment for 5 days. Therefore, after operating for continuous 48 h, the water flux is saturated at 25.7 L/m^2.h as compared to 28.5 L/m^2.h for a day of operation, see supplementary Fig. S7c-d.

4.3. Energy recovering in the FO process

The previous sections demonstrated that the VO-aSiO-rGO membrane exhibits remarkable performance in both concentration gradient-driven energy harvesting and the FO process. In the FO test cell, two Ag wires (connected to the sourcemeter through Cu wires) are placed in the FO test cell on either side of the membrane (active layer and support layer) to study the simultaneous electricity harvesting and FO process in ALDS mode. Fig. 4a and Fig. 4b shows the output voltage and output current as a function of time with 1 M KCl as DS and DI water as the FS. With equal DS and FS flow rate of 2 L/h, the constant output voltage of 290 mV is measured wherein the current is reduced from 30 μA to 27.8 μA during 2.4 h of continuous operation. The decrease in current over time can be attributed to factors such as accumulation of ions across the membrane and membrane clogging. The open-circuit voltage mainly depends on the permselectivity and concentration difference [13]. Since, the draw and feed solution concentrations are almost constant (in continuous mode), the open-circuit voltage exhibited a constant output throughout the experiment.

The comparison analysis of the energy and forward osmosis performance at different flow rates is also investigated. At a lower flow rate (0.5 L/h), the output voltage and current are 296 mV and 36 μA and simultaneously the water flux and RSF is measured to be around 12.8 L/m^2.h and 3.4 g/m^2.h, respectively. From the saturated voltage and current values (296 mV and 36 μA, respectively) the power output is calculated to be 0.026 W.m^{-2}. The energy consumption for pumping is calculated to be 0.100 W.m^{-2} by using the following Equation (2).

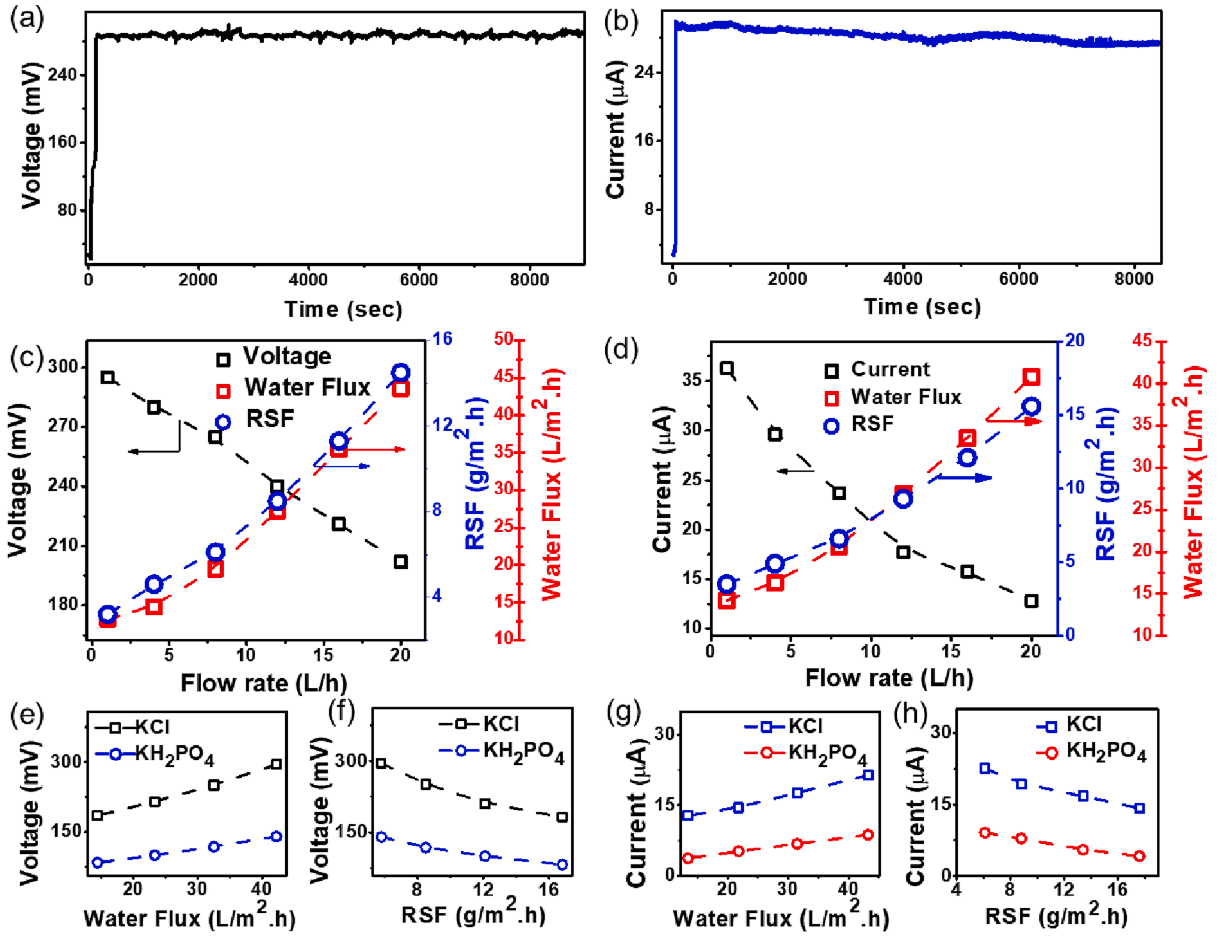

Fig. 4. Energy recovering in the FO process: Output (a) voltage, and (b) current of VO-aSiO-rGO membrane in continuous FO process (flow rate 2 L/h for both DS and FS). Comparison of (c) voltage, and (d) current with different FO parameters, at different flowrate in batch mode. 1 M KCl and DI water are used as DS and FS, respectively. Simultaneous energy harvesting and FO application with 1 M KCl and 1 M KH_2PO_4 as the DS in batch mode, (e) voltage vs water flux, (f) voltage vs RSF, (g) current vs water flux, and (h) current vs RSF, DI water is used as the FS.

$$P = (f^*Q^*\Delta P)/\eta^*A \quad (2)$$

Where Q is the flow rate (0.5 L/h), ΔP is the differential pressure measured to be 0.05 Psi, A is the membrane area, η is the pump efficiency ~ 0.7 and f is the conversion value (11.2^*10^{-4}) [13,54]. Based on the above parameters, overall energy saving in the FO process through concentration-driven electricity is calculated to be ~ 26 %.

To gain further insights into the synchronized energy harvesting and forward osmosis process, the flow rates of both the DS and FS sides are increased simultaneously. While both the flow rates (DS and FS sides) increased, the water flux and RSF increased from 12.8 L/m^2.h to 43.6 L/m^2.h and 3.4 g/m^2.h to 15.3 g/m^2.h, respectively. The observed variations in the water flux and RSF can be explained through variations in DECP and concentrative internal concentration polarization (CICP) with respect to DS and FS flow rate. The DECP at the active layer of the membrane reduces with an increase in DS flow rate and then will increase the DS concentration at the membrane surface [55]. Similarly, the CICP at the support layer reduces with an increase in FS flow rate, and that will reduce both DS and FS solute concentration at the interface between the support and separation layer and that will increase both water flux and RSF [56]. Even though, the RSF and water flux are increasing with flow rate, the output voltage and current are decreasing when flow rates are increased and this phenomena is observed due to reduced residence time of ions near the membrane surface, (refer Fig. 4c and Fig. 4d). Further similar response observed while increasing DS flow rate alone (Fig. 5a and Fig. 5b) confirms that DS resistance time is critical parameter to achieve optimum power output. As DI water is taken as FS, no CICP occurred at the support layer [55], but DS solute at interface between support and separation layer will be reduced with increase FS flow rate. The CICP on the support layer may have lighter effect on water flux and RSF, but the DECP on the active layer determines the output voltage and current values. Therefore, the output voltage and current values are found to be proportional to the salt rejection ability [13].

The effect of water flux and RSF on the output voltage and current in ALDS mode and batch mode is also studied for the VO-aSiO-rGO membrane by using 1 M KCl and 1 M KH_2PO_4 as the DS and DI water as the FS at constant DS and FS flow rates of 10 L/h and 15 L/h, respectively. As can be seen from Fig. 4e and Fig. 4f, the water flux of KCl is found to be higher than KH_2PO_4 due to the higher osmotic concentration gradient of KCl across the membrane surface [57], which is also evident from the osmotic pressure calculations shown in Table S1 in the supplementary section. Regarding the energy performance, the output voltage decreases with the decreasing water flux and increasing RSF for both KCl and KH_2PO_4. Similarly, the current values also decreased with decreasing water flux and increasing RSF, see Fig. 4g and Fig. 4h. The above observation suggests that good selectivity and permeability of membrane support both FO and electricity generation process. As mentioned earlier, detailed understandings of the interdependence of FO and concentration gradient-driven electricity harvesting process under the conditions of flowing electrolytes across the electrodes and membrane surfaces demand further theoretical studies. Since, the experiment is performed in batch mode, the osmotic pressure across the

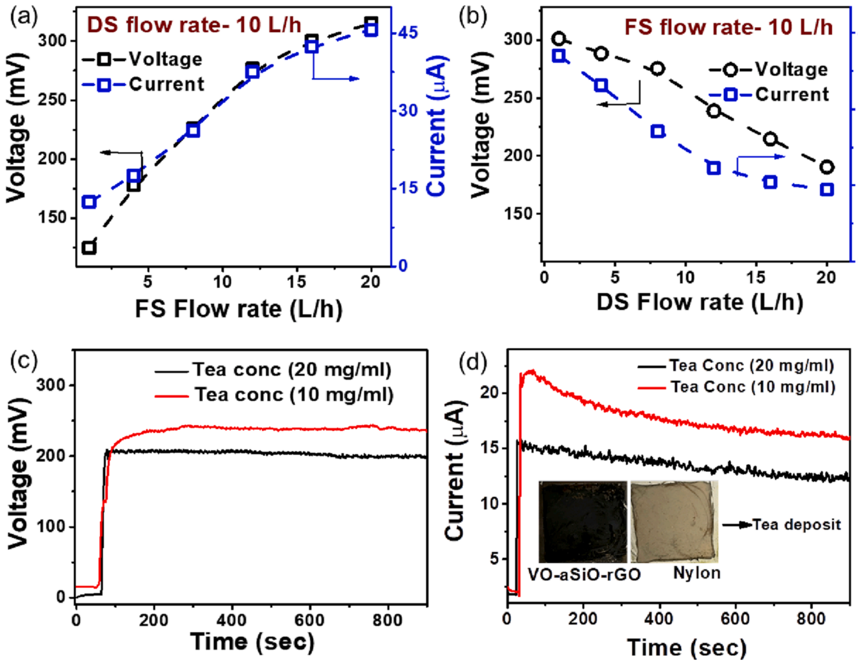

Fig. 5. Energy performance of VO-aSiO-rGO membrane: Effect of (a) varying DS flowrates with constant FS flowrates of 10 L/h, and (b) varying FS flowrates with constant DS flowrates of 10 L/h on current and voltage output. Output (c) voltage, and (d) current with 10 mg/ml and 20 mg/ml tea solutions used as the FS, 1 M KCl is used as the DS, (flowrate = 0.5 L/h on both sides). Digital images of the active and support layer after the experiment are shown in the inset of (d).

membrane decreased with DS dilution that decreased the water flux and increased the RSF value with time. As a result, both voltage and current decreased with time [58].

The effect of different flow rates of DS (at a constant flow rate of FS) and FS (at a constant flow rate of DS) flow rates on energy performance is also investigated in the ALDS mode. As can be seen from Fig. 5a, with increasing DS flow rates (by maintaining a constant FS flow rate), both output voltage and current decreased. This is because, at higher DS flowrates, the DECP and residence time will be reducing that will disrupt the ion equilibrium at the membrane surface, which in turn, reduces the ion transport through the membrane. This reduces the effective driving force of the draw solution and hence reduce both output voltage and current [59]. In contrast, when the FS flow rates are increased with a constant DS flow rate (Fig. 5b), both output voltage and current increased. This is because, at higher FS flow rates, the CICP has negligible effect, since DI water is used as FS. This improves the effective ionic transport through the membrane and reduces the RSF value to a great extent, thus maintaining the osmotic pressure across the membrane which will let to increase in both output voltage and current.

Finally, to check the applicability in real application scenario, thus fabricated membrane is explored for tea concentration and energy recovery in the FO process near its saturation point. Long term water flux performance is studied by using 1 M KCl as DS and tea solution (20 mg/ml) as the FS, flow rates are maintained at 10 L/h and 15 L/h, respectively. The membrane exhibited a water flux of 30 L/m^2.h for 2 h which gradually decreased with time and saturated at 12.5 L/m^2.h after 20 h continuous operation, thus increasing the tea concentration over time. The decreased water flux is attributed to the accumulation of tea molecules on the membrane surface (fouling) decreasing the mass transfer coefficient. This FO-based concentrating process leads to nucleation of tea crystals near the membrane [20,60], as shown in supplementary Fig. S13a-c. The FTIR spectra of brewed tea sample in Fig. S13b is consistent with the reported literatures revealing the presence of carboxylic acid, and aliphatic amine group [61].

This realistic scenario of tea concentrating through FO process is also explored for simultaneous energy recovering. Tea solutions of different concentrations (10 mg/ml and 20 mg/ml concentrations) are used as the FS, the optimized VO-aSiO-rGO is used as the FO membrane with 1 M KCl as the DS. The experiment is performed in the ALDS mode. Fig. 5c and Fig. 5d show the output voltage and current as a function of time with flow rates of DS and FS maintained at 0.5 L/h. The output saturated voltage (240 mV and 205 mV) and current (17 μA, and 13.5 μA) obtained with 10 and 20 mg/ml tea solutions as FS is found to be lower than that of DI water as the FS (296 mV and 36 μA). This is because the inorganic ions present in the tea solution could neutralize the concentration gradient-driven permselective movements of ions. Moreover, at higher feed concentration compared to DI water, the mass transfer coefficient decreases due to the effect of CICP, which in turn decreases the net osmotic pressure across the membrane [62]. By emphasizing the application of the membrane in tea concentration and energy generation, we aim to showcase its potential for use in industries related to tea processing and potentially in other applications that require concentration processes and energy harvesting.

Further studies related to the effects of different membrane

Table 3
Comparison of energy efficiency for different DS solutions at the lowest flow rate.

Molarity (M)	DS/FS flow rates (L/h)	Voltage (mV)	Current (μA)	Extracted Power (W.m^{-2})	Pumping Power (W.m^{-2})	Saving Energy (%)
1 M KCl	0.5	295	35	0.0258	0.10	25.8
2 M KCl	0.5	340	48.5	0.041	0.10	41
3 M KCl	0.5	380	62	0.0589	0.10	58.9
1 M NaCl	0.5	280	20	0.014	0.10	14
1 M $MgCl_2$	0.5	240	13.5	0.0081	0.10	8.1
1 M KH_2PO_4	0.5	135	8.5	0.00286	0.10	2.86

materials, different draw solute concentrations, increasing KCl molarity and increasing flow rates on the energy harvesting process in ALDS mode of FO setup are discussed in the supplementary section in Fig. S10a-b, Fig. S11a-d and Fig. S12a-b, respectively. Table 3 represents the comparison of energy efficiency for different draw solutions.

5. Conclusion

In conclusion, we demonstrated the possibility of synchronized energy harvesting in the FO process with an overall energy saving of ~ 26 %. The robust nanofluidic FO membrane fabricated by crosslinking 2D flakes of VO and rGO extracted electrical power (up to 4.72 $W.m^{-2}$) from the concentration gradient. The FO performance of the VO-aSiO-rGO membrane (45 $L/m^2.h$) is found to be better than that of both the pristine rGO membrane (26 $L/m^2.h$) and commercial CTA-FO membrane (7.8 $L/m^2.h$). The membrane reported here showed outstanding long-term stability in both acidic and basic mediums (for more than 90 days of soaking) as well as during prolonged operational 40 h of the FO without showing any sign of leaching. The possibility of extracting electrical energy from realistic FO processes is demonstrated by using DI water and tea solutions as the FS. It is observed that in the continuous FO mode, the system is able to generate constant output voltage (290 mV) and current (28 μA) for prolonged operational 2.4 h. Moreover, in batch mode, the system is able to generate highest output voltage and current of 296 mV and 36 μA, respectively while simultaneously producing water flux of 12.8 $L/m^2.h$ and RSF of 3.4 $g/m^2.h$ at 0.5 L/h flow rates. Finally, the FO system is able to produce tea crystals and generate electrical output voltage and current with different tea concentrations. Considering the ease of coupling between FO and concentration gradient-driven energy harvesting process, this study could lead to a novel platform for studying or handling the highly entangled issues water-energy nexus and creating a self-sustaining system that can operate independently of external energy sources.

Declaration of Competing Interest

The authors declare the following financial interests/personal relationships which may be considered as potential competing interests: Dr. Kalyan Raidongia reports financial support was provided by Department of Science and Technology, Government of India.

Data availability

Data will be made available on request.

Acknowledgement

The authors would like to acknowledge the Science and Engineering Research Board, India, for financial support (project number: CRG/2020/002943). The authors would also like to acknowledge the Central Instrumental Facility (CIF) for helping with sample characterization. The authors would also like to thank the Department of Chemistry for using the FTIR spectrophotometer for analysis.

Appendix A. Supplementary data

Supplementary data to this article can be found online at https://doi.org/10.1016/j.cej.2023.143964.

References

[1] W.L. Ang, A. Wahab Mohammad, D. Johnson, N. Hilal, Forward osmosis research trends in desalination and wastewater treatment: A review of research trends over the past decade, Journal of Water, Process. Eng. 31 (2019), 100886, https://doi.org/10.1016/j.jwpe.2019.100886.

[2] K. Li, M. Li, W. Zhang, Y. Xue, Z. Wang, X. Zhang, A Staged Forward Osmosis Process for Simultaneous Desalination and Concentration of Textile Wastewaters, ACS ES&T Water. (2022), https://doi.org/10.1021/acsestwater.2c00314.

[3] S. Vinardell, S. Astals, J. Mata-Alvarez, J. Dosta, Techno-economic analysis of combining forward osmosis-reverse osmosis and anaerobic membrane bioreactor technologies for municipal wastewater treatment and water production, Bioresour. Technol. 297 (2020), 122395, https://doi.org/10.1016/j.biortech.2019.122395.

[4] M. Szczygiełda, M. Krajewska, A. Andrzejewski, L. Zheng, L.D. Nghiem, P. Oleskowicz-Popiel, D. Szymanowska, K. Prochaska, Dewatering fermentation broth for keto carboxylic acid enrichment by forward osmosis: A techno-economic analysis, J. Membr. Sci. 679 (2023), 121699, https://doi.org/10.1016/j.memsci.2023.121699.

[5] N. Akther, A. Sodiq, A. Giwa, S. Daer, H.A. Arafat, S.W. Hasan, Recent advancements in forward osmosis desalination: A review, Chem. Eng. J. 281 (2015) 502–522, https://doi.org/10.1016/j.cej.2015.05.080.

[6] M. Giagnorio, F. Ricceri, A. Tiraferri, Desalination of brackish groundwater and reuse of wastewater by forward osmosis coupled with nanofiltration for draw solution recovery, Water Res. 153 (2019) 134–143, https://doi.org/10.1016/j.watres.2019.01.014.

[7] S.K. Singh, C. Sharma, A. Maiti, A comprehensive review of standalone and hybrid forward osmosis for water treatment: Membranes and recovery strategies of draw solutions, J. Environ. Chem. Eng. 9 (2021), 105473, https://doi.org/10.1016/j.jece.2021.105473.

[8] N.K. Rastogi, Opportunities and Challenges in Application of Forward Osmosis in Food Processing, Crit. Rev. Food Sci. Nutr. 56 (2016) 266–291, https://doi.org/10.1080/10408398.2012.724734.

[9] L. Yu, B. Jiang, Z. Yang, D. Chen, Y. Yuan, X. Fan, Y. Yu, Development of high-performance electrospun nanofiber based forward osmosis membrane by introducing graphene oxide-calcium carbonate particle composite intermediate layer, Desalination 531 (2022), 115672, https://doi.org/10.1016/j.desal.2022.115672.

[10] X. Tong, S. Liu, Y. Zhao, C. Xiao, Y. Chen, J. Crittenden, A freestanding graphene oxide framework membrane for forward osmosis: Separation performance and transport mechanistic insights, J. Membr. Sci. 661 (2022), 120919, https://doi.org/10.1016/j.memsci.2022.120919.

[11] T. Cai, N. Jiang, G. Zhen, L. Meng, J. Song, G. Chen, Y. Liu, M. Huang, Simultaneous energy harvest and nitrogen removal using a supercapacitor microbial fuel cell, Environ. Pollut. 266 (2020), 115154, https://doi.org/10.1016/j.envpol.2020.115154.

[12] M. Tawalbeh, A. Al-Othman, K. Singh, I. Douba, D. Kabakebji, M. Alkasrawi, Microbial desalination cells for water purification and power generation: A critical review, Energy 209 (2020), 118493, https://doi.org/10.1016/j.energy.2020.118493.

[13] C.H. Park, O. Choi, Electrochemical energy-generating desalination system using a pressure-driven ion-selective nanomembrane, Nano Energy 94 (2022), 106939, https://doi.org/10.1016/j.nanoen.2022.106939.

[14] A.M. Dafalla, L. Wei, B.T. Habte, J. Guo, F. Jiang, Membrane Electrode Assembly Degradation Modeling of Proton Exchange Membrane Fuel Cells: A Review, Energies 15 (23) (2022) 9247.

[15] G. Wei, Y. Wang, C. Huang, Q. Gao, Z. Wang, L. Xu, The stability of MEA in SPE water electrolysis for hydrogen production, Int. J. Hydrogen Energy 35 (2010) 3951–3957, https://doi.org/10.1016/j.ijhydene.2010.01.153.

[16] N.Y. Yip, A. Tiraferri, W.A. Phillip, J.D. Schiffman, L.A. Hoover, Y.C. Kim, M. Elimelech, Thin-Film Composite Pressure Retarded Osmosis Membranes for Sustainable Power Generation from Salinity Gradients, Environ. Sci. Tech. 45 (2011) 4360–4369, https://doi.org/10.1021/es104325z.

[17] J.G. Hong, B. Zhang, S. Glabman, N. Uzal, X. Dou, H. Zhang, X. Wei, Y. Chen, Potential ion exchange membranes and system performance in reverse electrodialysis for power generation: A review, J. Membr. Sci. 486 (2015) 71–88, https://doi.org/10.1016/j.memsci.2015.02.039.

[18] B. Yang, J. Yu, T. Ma, A charge-free and membrane-free hybrid capacitive mixing system for salinity gradient energy harvesting, J. Mater. Chem. A 11 (7) (2023) 3388–3398.

[19] H.M. Hegab, A. ElMekawy, T.G. Barclay, A. Michelmore, L. Zou, C.P. Saint, M. Ginic-Markovic, Effective in-situ chemical surface modification of forward osmosis membranes with polydopamine-induced graphene oxide for biofouling mitigation, Desalination 385 (2016) 126–137, https://doi.org/10.1016/j.desal.2016.02.021.

[20] P. Deka, V.K. Verma, A. Chandrasekaran, A.B. Neog, A. Bardhan, K. Raidongia, S. Subbiah, Performance of novel sericin doped reduced graphene oxide membrane for FO based membrane crystallization application, J. Membr. Sci. 660 (2022), 120884, https://doi.org/10.1016/j.memsci.2022.120884.

[21] R. Gogoi, H. Madeshwaran, A. Ghosh, Y. Green, K. Raidongia, Ionic Thermoelectric Properties of Reconstructed Lamellar Vanadium Pentoxide Membranes, Advanced Functional Materials. n/a (2023) 2301178, https://doi.org/10.1002/adfm.202301178.

[22] R.K. Gogoi, A.B. Neog, T.J. Konch, N. Sarmah, K. Raidongia, A two-dimensional ion-pump of a vanadium pentoxide nanofluidic membrane, J. Mater. Chem. A 7 (2019) 10552–10560, https://doi.org/10.1039/c8ta11233a.

[23] Z. Zhao, S. Ni, X. Su, Y. Gao, X. Sun, Thermally Reduced Graphene Oxide Membrane with Ultrahigh Rejection of Metal Ions' Separation from Water, ACS Sustain. Chem. Eng. 7 (2019) 14874–14882, https://doi.org/10.1021/acssuschemeng.9b02972.

[24] E. Yang, A.B. Alayande, C.-M. Kim, J. Song, I.S. Kim, Laminar reduced graphene oxide membrane modified with silver nanoparticle-polydopamine for water/ion

separation and biofouling resistance enhancement, Desalination 426 (2018) 21–31, https://doi.org/10.1016/j.desal.2017.10.023.

[25] K. Rambabu, F. Banat, Q.M. Pham, S.-H. Ho, N.-Q. Ren, P.L. Show, Biological remediation of acid mine drainage: Review of past trends and current outlook, Environ. Sci. Ecotechnol. 2 (2020), 100024, https://doi.org/10.1016/j.ese.2020.100024.

[26] K.W. Chew, J.Y. Yap, P.L. Show, N.H. Suan, J.C. Juan, T.C. Ling, D.-J. Lee, J.-S. Chang, Microalgae biorefinery: High value products perspectives, Bioresour. Technol. 229 (2017) 53–62, https://doi.org/10.1016/j.biortech.2017.01.006.

[27] K.S. Khoo, K.W. Chew, G.Y. Yew, W.H. Leong, Y.H. Chai, P.L. Show, W.-H. Chen, Recent advances in downstream processing of microalgae lipid recovery for biofuel production, Bioresour. Technol. 304 (2020), 122996, https://doi.org/10.1016/j.biortech.2020.122996.

[28] S.Y. Cheng, X. Tan, P.L. Show, K. Rambabu, F. Banat, A. Veeramuthu, B.F. Lau, E. P. Ng, T.C. Ling, Incorporating biowaste into circular bioeconomy: A critical review of current trend and scaling up feasibility, Environ. Technol. Innov. 19 (2020), 101034, https://doi.org/10.1016/j.eti.2020.101034.

[29] C.J. Fontenot, J.W. Wiench, M. Pruski, G.L. Schrader, Vanadia Gel Synthesis via Peroxovanadate Precursors. 1. In Situ Laser Raman and 51 V NMR Characterization of the Gelation Process, J. Phys. Chem. B 104 (49) (2000) 11622–11631.

[30] J. Deka, K. Saha, R. Gogoi, G.K. Dutta, K. Raidongia, Fabrication of Pressure-Responsive Energy Device from Nanofluidic Vanadium Pentoxide and Polymeric Hydrogel, ACS Appl. Electronic Mater. 3 (2021) 277–284, https://doi.org/10.1021/acsaelm.0c00849.

[31] P. Taylor, M. Kusper, T. Hesabizadeh, L.D. Geoffrion, F. Watanabe, E. Herth, G. Guisbiers, Synthesis of naked vanadium pentoxide nanoparticles, Nanoscale Adv. 3 (2021) 1954–1961, https://doi.org/10.1039/D1NA00029B.

[32] M. Li, C. Liu, Y. Xie, H. Cao, H. Zhao, Y. Zhang, The evolution of surface charge on graphene oxide during the reduction and its application in electroanalysis, Carbon 66 (2014) 302–311, https://doi.org/10.1016/j.carbon.2013.09.004.

[33] H. Cheng, Y. Zhou, Y. Feng, W. Geng, Q. Liu, W. Guo, L. Jiang, Electrokinetic Energy Conversion in Self-Assembled 2D Nanofluidic Channels with Janus Nanobuilding Blocks, Adv. Mater. 29 (2017) 1700177, https://doi.org/10.1002/adma.201700177.

[34] M. Fantauzzi, B. Elsener, D. Atzei, A. Rigoldi, A. Rossi, Exploiting XPS for the identification of sulfides and polysulfides, RSC Adv. 5 (2015) 75953–75963, https://doi.org/10.1039/C5RA14915K.

[35] M. Marrone, T. Montanari, G. Busca, L. Conzatti, G. Costa, M. Castellano, A. Turturro, A Fourier Transform Infrared (FTIR) Study of the Reaction of Triethoxysilane (TES) and Bis[3-triethoxysilylpropyl]tetrasulfane (TESPT) with the Surface of Amorphous Silica, J. Phys. Chem. B 108 (2004) 3563–3572, https://doi.org/10.1021/jp036148x.

[36] Q. Tian, Y. Tang, T. Ding, X. Li, Z. Zhang, Effect of nano-silica surface-capped by bis[3-(triethoxysilyl)propyl] tetrasulfide on the mechanical properties of styrene-butadiene rubber/butadiene rubber nanocomposites, Composites, Communications 10 (2018) 190–193, https://doi.org/10.1016/j.coco.2018.10.005.

[37] Y.-H. Xi, J.-Q. Hu, Z. Liu, R. Xie, X.-J. Ju, W. Wang, L.-Y. Chu, Graphene Oxide Membranes with Strong Stability in Aqueous Solutions and Controllable Lamellar Spacing, ACS Appl. Mater. Interfaces 8 (24) (2016) 15557–15566.

[38] P. Deka, V.K. Verma, B. Yurembam, A.B. Neog, K. Raidongia, S. Subbiah, Performance evaluation of reduced graphene oxide membrane doped with polystyrene sulfonic acid for forward osmosis process, Sustainable Energy Technol. Assess. 44 (2021), 101093, https://doi.org/10.1016/j.seta.2021.101093.

[39] W.L. Zhang, H.J. Choi, Silica-Graphene Oxide Hybrid Composite Particles and Their Electroresponsive Characteristics, Langmuir 28 (2012) 7055–7062, https://doi.org/10.1021/la3009283.

[40] B. Kim, G. Gwak, S. Hong, Review on methodology for determining forward osmosis (FO) membrane characteristics: Water permeability (A), solute permeability (B), and structural parameter (S), Desalination 422 (2017) 5–16, https://doi.org/10.1016/j.desal.2017.08.006.

[41] W. Wang, J. Hao, Q. Sun, M. Zhao, H. Liu, C. Li, X. Sui, Carbon nanofibers membrane bridged with graphene nanosheet and hyperbranched polymer for high-performance osmotic energy harvesting, Nano Res. 16 (2023) 1205–1211, https://doi.org/10.1007/s12274-022-4634-6.

[42] S. Zhou, L. Xie, L. Zhang, L. Wen, J. Tang, J. Zeng, T. Liu, D. Peng, M. Yan, B. Qiu, Q. Liang, K. Liang, L. Jiang, B. Kong, Interfacial Super-Assembly of Ordered Mesoporous Silica-Alumina Heterostructure Membranes with pH-Sensitive Properties for Osmotic Energy Harvesting, ACS Appl. Mater. Interfaces 13 (2021) 8782–8793, https://doi.org/10.1021/acsami.0c21661.

[43] N. Sheng, S. Chen, M. Zhang, Z. Wu, Q. Liang, P. Ji, H. Wang, TEMPO-Oxidized Bacterial Cellulose Nanofibers/Graphene Oxide Fibers for Osmotic Energy Conversion, ACS Appl. Mater. Interfaces 13 (2021) 22416–22425, https://doi.org/10.1021/acsami.1c03192.

[44] T.J. Konch, T. Dutta, A.B. Neog, R. Gogoi, K. Raidongia, Uphill Anion Pumping through Triangular Nanofluidic Device of Reconstructed Layered Double Hydroxide, J. Phys. Chem. C 125 (2021) 17939–17949, https://doi.org/10.1021/acs.jpcc.1c03118.

[45] R. Qin, J. Tang, C. Wu, Q. Zhang, T. Xiao, Z. Liu, Y. Jin, J. Liu, H. Wang, Nanofiber-reinforced clay-based 2D nanofluidics for highly efficient osmotic energy harvesting, Nano Energy 100 (2022), 107526, https://doi.org/10.1016/j.nanoen.2022.107526.

[46] Z. Gao, J. Zhang, M. Ahmad, B. Jiang, Z. Sun, S. Wang, Y. Jin, Design of metallic phase WS2/cellulose nanofibers composite membranes for light-boosted osmotic energy conversion, Carbohydr. Polym. 296 (2022), 119847, https://doi.org/10.1016/j.carbpol.2022.119847.

[47] P. Liu, Y. Sun, C. Zhu, B. Niu, X. Huang, X.-Y. Kong, L. Jiang, L. Wen, Neutralization Reaction Assisted Chemical-Potential-Driven Ion Transport through Layered Titanium Carbides Membrane for Energy Harvesting, Nano Lett. 20 (2020) 3593–3601, https://doi.org/10.1021/acs.nanolett.0c00526.

[48] J. Gao, W. Guo, D. Feng, H. Wang, D. Zhao, L. Jiang, High-Performance Ionic Diode Membrane for Salinity Gradient Power Generation, J. Am. Chem. Soc. 136 (2014) 12265–12272, https://doi.org/10.1021/ja503692z.

[49] P. Jia, X. Du, R. Chen, J. Zhou, M. Agostini, J. Sun, L. Xiao, The Combination of 2D Layered Graphene Oxide and 3D Porous Cellulose Heterogeneous Membranes for Nanofluidic Osmotic Power Generation, Molecules 26 (17) (2021) 5343.

[50] J. Feng, M. Graf, K. Liu, D. Ovchinnikov, D. Dumcenco, M. Heiranian, V. Nandigana, N.R. Aluru, A. Kis, A. Radenovic, Single-layer MoS2 nanopores as nanopower generators, Nature 536 (2016) 197–200, https://doi.org/10.1038/nature18593.

[51] D.R. Paul, Reformulation of the solution-diffusion theory of reverse osmosis, J. Membr. Sci. 241 (2004) 371–386, https://doi.org/10.1016/j.memsci.2004.05.026.

[52] A. Bhinder, S. Shabani, M. Sadrzadeh, Effect of Internal and External Concentration Polarizations on the Performance of Forward Osmosis Process, Osmotically Driven Membrane Processes - Approach, in: H. Du, A. Thompson, X. Wang (Eds.), Osmotically Driven Membrane Processes - Approach, Development and Current Status, InTech, 2018.

[53] A. Bhinder, S. Shabani, M. Sadrzadeh, Effect of Internal and External Concentration Polarizations on the Performance of Forward Osmosis Process, in (2018), https://doi.org/10.5772/intechopen.71343.

[54] T.M. Mansour, T.M. Ismail, K. Ramzy, M. Abd El-Salam, Energy recovery system in small reverse osmosis desalination plant: Experimental and theoretical investigations, Alex. Eng. J. 59 (2020) 3741–3753, https://doi.org/10.1016/j.aej.2020.06.030.

[55] G.T. Gray, J.R. McCutcheon, M. Elimelech, Internal concentration polarization in forward osmosis: role of membrane orientation, Desalination 197 (2006) 1–8, https://doi.org/10.1016/j.desal.2006.02.003.

[56] D. Dsilva Winfred Rufuss, E. Hosseinipour, S. Arulvel, P.A. Davies, Complete parametric investigation of a forward osmosis process using sodium chloride draw solution, Desalination 547 (2023), 116218.

[57] D.u. Bai, B. Kruczek, Effect of Membrane Orientation and Concentration of Draw Solution on the Behavior of Commercial Osmotic Membrane in a Novel Dynamic Forward Osmosis Tests, Membranes 12 (4) (2022) 385.

[58] Y.C. Kim, Y. Kim, D. Oh, K.H. Lee, Experimental Investigation of a Spiral-Wound Pressure-Retarded Osmosis Membrane Module for Osmotic Power Generation, Environ. Sci. Tech. 47 (2013) 2966–2973, https://doi.org/10.1021/es304060d.

[59] J.R. McCutcheon, M. Elimelech, Influence of concentrative and dilutive internal concentration polarization on flux behavior in forward osmosis, J. Membr. Sci. 284 (2006) 237–247, https://doi.org/10.1016/j.memsci.2006.07.049.

[60] A. Bardhan, S. Subbiah, K. Mohanty, Modeling and Experimental Validation for the Preparation of Concentrated Tea Extract Using a Forward Osmosis Process Using a Food-Grade Inorganic Draw Solute, Ind. Eng. Chem. Res. 62 (2023) 3315–3326, https://doi.org/10.1021/acs.iecr.2c04219.

[61] M. Brza, S.B. Aziz, H. Anuar, F. Ali, E. Dannoun, S. Jalal, R. Abdulwahid, S. Al-Zangana, Tea from the drinking to the synthesis of metal complexes and fabrication of PVA based polymer composites with controlled optical band gap, Sci. Rep. 10 (2020) 18108, https://doi.org/10.1038/s41598-020-75138-x.

[62] S. Phuntsho, S. Sahebi, T. Majeed, F. Lotfi, J.E. Kim, H.K. Shon, Assessing the major factors affecting the performances of forward osmosis and its implications on the desalination process, Chem. Eng. J. 231 (2013) 484–496, https://doi.org/10.1016/j.cej.2013.07.058.